Journal of Wind Engineering & Industrial Aerodynamics 247 (2024) 105681

Contents lists available at ScienceDirect

Journal of Wind Engineering & Industrial Aerodynamics

journal homepage: www.elsevier.com/locate/jweia

A nonlinear approach for the simulation of the buffeting response of long span bridges under non-synoptic storm winds

Filippo Calamelli, Roberto Rossi, Tommaso Argentini *, Daniele Rocchi, Giorgio Diana

Politecnico di Milano, Department of Mechanical Engineering, via La Masa 1, 20156 Milano, Italy

ARTICLE INFO

Keywords:
Nonlinear rheological model
Non-synoptic wind
Buffeting response
Long-span bridges

ABSTRACT

In recent years, extreme atmospheric events are becoming increasingly frequent and unpredictable. These phenomena are often characterized by low-frequency variations of the wind speed and angle of attack, mainly due to large-scale turbulence. These features can be critical for long-span bridges as they can lead the deck in conditions where the nonlinear effects of aerodynamic forces are enhanced. Therefore, it is increasingly important to develop reliable numerical tools to simulate the response of these structures to non-synoptic winds. In this work, a nonlinear rheological model that is able to account for the large variations in wind speed and angle of attack is employed to investigate the dynamic response of two different bridges subjected to two different wind fields. The first scenario is a standard synoptic wind field used as a baseline. On the other hand, the second wind scenario represents an extreme non-synoptic atmospheric event. The results highlight how the nonlinear effects of the aerodynamic forces, in particular those related to the large variation of the angle of attack, could lead to significant changes in the bridges' response. These effects would not be captured by employing standard linearized methods.

1. Introduction

In the current era, increasingly longer and longer suspension bridges are being constructed. As a consequence, there is a growing need for a reliable numerical model that can accurately predict the behavior of these structures when subjected to turbulent wind conditions. Besides the structural challenges, an additional complication arises from the increasing occurrence of non-synoptic climate events, which may exhibit sudden variations in wind speed, non-horizontal or skewed wind directions, and severe turbulence conditions (e.g. Andersen et al., 2022; Fenerci and Øiseth, 2018; Burlando et al., 2017; Wang et al., 2016). These features are different from those typical of standard synoptic phenomena, which are described and included in existing codes and standards. The emphasis of this research is on non-synoptic events, specifically storms and downbursts. Other phenomena, such as tornadoes, are beyond the scope of the present investigation. Creating a numerical model to accurately predict the wind forces associated to these atmospheric events, and their nonlinear effects on a bridge deck, remains an outstanding challenge (Hao and Wu, 2017).

The standard approaches, used to estimate the aerodynamic response of a bridge, consist of a linearization of the forces around the static equilibrium position of the deck subjected to a mean wind speed. As a result, the wind loads can be expressed by superimposing to the static contribution the self-excited and the buffeting forces, which can be defined respectively identifying the flutter derivatives and the admittance functions. Based on these assumptions, in the last decades, several methods were developed in both time and frequency domain (e.g. Davenport, 1962; Scanlan, 1987; Caracoglia and Jones, 2003; Chen et al., 2000; Chen and Kareem, 2001; Kavrakov and Morgenthal, 2017; Kavrakov et al., 2019; Jain et al., 1996; Øiseth et al., 2010; Øiseth and Sigbjörnsson, 2011; Øiseth et al., 2012; Stoyanoff, 2001; Argentini et al., 2014, 2016; Diana et al., 2015a; Katsuchi et al., 1999; Montoya et al., 2020; Minh et al., 1999).

The first part of the benchmark study proposed by the IABSE Task Group 3.1 (Diana et al., 2020a,b, 2022) focused on comparing and validating different linear numerical approaches. The results highlighted that, despite some discrepancies, there is quite good agreement between the methods used. On the other hand, when nonlinear approaches are considered, the uncertainties increase.

These differences become even more evident when non-synoptic features are introduced in the incoming turbulent wind field. Indeed, full-scale measurements have shown that atmospheric winds can exhibit low-frequency variations in the angle of attack, primarily attributed to large-scale turbulence. In studies such as Andersen et al. (2022) on the Gjemnessund Bridge and Fenerci and Øiseth (2018) on the Hardanger Bridge in Norway, severe angles of attack, along with

* Corresponding author.
E-mail address: tommaso.argentini@polimi.it (T. Argentini).

https://doi.org/10.1016/j.jweia.2024.105681
Received 21 August 2023; Received in revised form 31 January 2024; Accepted 15 February 2024
0167-6105/© 2024 The Author(s). Published by Elsevier Ltd. This is an open access article under the CC BY license (http://creativecommons.org/licenses/by/4.0/).

Table 1
List of the main symbols employed.

B	Deck chord	[m]
ρ	Air density	[kg m^{-3}]
U	Along-wind mean wind speed	[m s^{-1}]
f	Frequency	[Hz]
f^*	Reduced frequency $f^* = \frac{fB}{U}$	[−]
V^*	Reduced velocity $V^* = \frac{1}{f^*}$	[−]
y	Horizontal displacement	[m]
z	Vertical displacement	[m]
θ	Torsional rotation	[°]
u	Along-wind turbulence component	[m s^{-1}]
w	Vertical turbulence component	[m s^{-1}]
AoA	Wind angle of attack $AoA = \arctan(\frac{w}{u})$	[°]
D	Drag force per unit length	[N m^{-1}]
L	Lift force per unit length	[N m^{-1}]
M	Pitching moment per unit length	[N]
f_{cut}	Corrected Quasi-Steady Theory (CQST) cutoff frequency	[Hz]
V^*_{cut}	CQST limiting reduced velocity	[−]
$V_{rel,j}$	CQST relative velocity, $j = D, L, M$	[m s^{-1}]
ψ_j	Rotation of $V_{rel,j}$ with respect to the horizontal, $j = D, L, M$	[°]
α_j	CQST effective wind angle of attack, $j = D, L, M$	[°]
$B_{1,j}$	CQST correction coefficients, $j = D, L, M$	[−]

sudden variations in mean wind speed, were recorded. These findings highlight the significance of considering non-synoptic features in the analysis of wind effects on bridges. The presence of large variations in wind conditions can lead to complex dynamic responses since the hypothesis of small oscillations around the static deformation of the bridge deck is no longer valid.

In these turbulent wind conditions, the nonlinear dependence of aerodynamic forces on both the reduced velocity V^* (in this work, the reduced velocity is defined as $V^* = \frac{U}{fB}$, where U is the mean wind speed, f is the frequency of the bridge motion and the B is the length of the deck chord) and the variation of the wind angle of attack α must be taken into consideration. As a result, researchers have been exploring methods to introduce nonlinear features into their procedures for simulating the buffeting response of bridges.

Diana et al. (2008) introduced a nonlinear rheological approach to model the hysteresis loops of self-excited and buffeting forces. This approach involves a composition of simple linear and nonlinear mechanical systems, each expressing a relationship between forces and angle of attack. This model offers a more accurate representation of the nonlinear effects observed in turbulent wind conditions. Subsequently, in Diana et al. (2010), the model was further enhanced by describing the hysteresis loops using a polynomial function of the angle of attack.

Wu and Kareem (2014) introduced a Volterra model wherein, presenting a different perspective, aerodynamic forces were expressed as a combination of linear and higher-order convolutions. These high-order kernels, though capable of considering nonlinearities in quasi-steady and unsteady effects, came with the drawback of demanding significant computational resources for their determination. To address this computational challenge, the number of high-order kernels was reduced, selectively choosing them based on physical considerations. The method was specifically tested on twin-box sections by Skyvulstad et al. (2021b, 2023). Indeed, these sections are known to usually exhibit a nonlinear dependence of aerodynamic coefficients upon the angle of attack, as demonstrated in studies such as Skyvulstad et al. (2021a) and Argentini et al. (2022).

In a separate study, still focusing on twin-box decks, Zhou et al. (2018) introduced a new category of parametric nonlinear approaches for modeling aerodynamic forces. Their method involved a nonlinear differential equation formulated in a generalized state-space form. The resulting reduced-order models displayed high flexibility in replicating behavior observed in experiments. However, due to the large number of parameters involved, these models were challenging to be interpreted physically.

There is another class of models based on the classical Quasi Steady Theory (QST). The QST is the only nonlinear analytical method to predict aerodynamic forces as a function of bridge motion and wind turbulence. Nevertheless, the QST may not fully match experimental results at high V^* values. This discrepancy can lead to inaccuracies in predicting aerodynamic torsional damping. Therefore, Diana et al. (1995) introduced the "corrected" QST method (CQST) to better capture the aerodynamic forces at high V^*.

Unfortunately, it is well-known that the CQST accurately predicts wind forces only for high values of the reduced velocity. The threshold value of V^* is typically set between 15 and 25 and it depends on the aerodynamic properties of the bridge studied. A criterion to define the limiting V^* is to consider a reduced velocity above which the flutter derivatives almost converge to the corresponding quasi-steady limit. Therefore, to account for the nonlinearities of the aerodynamic forces at low V^*, Diana et al. (2013) proposed a dual-band strategy based on the classical "band superposition" approach outlined by Diana et al. (1995). The method consists in dividing the atmospheric wind spectrum in a low-frequency range (LF band) and a high-frequency range (HF band). Specifically, considering the LF part, the CQST can be used to predict the aerodynamic forces including the nonlinearities due to the large scales of turbulence, since the dependence on V^* is negligible. On the other hand, the HF non-linear effects are modeled linearizing around the LF solution. Finally, the total response is obtained by superimposing the two contributions.

Several approaches were proposed in the literature to linearize the aerodynamic forces at HF around the slow-varying LF solution. The method outlined by Diana et al. (2013) was recently updated in Diana and Omarini (2020), where rheological models were employed to correct the CQST over the full range of V^*, therefore avoiding the problem of selecting a threshold for the HF band. However, the application of this approach is not straightforward since the resulting HF models are often characterized by inherently unstable behavior. This model has been successfully applied in a few case studies, including the Izmit Bay Bridge (Argentini et al., 2020) and the Third Bosphorus Bridge (Diana and Omarini, 2020).

Alternatively, Chen and Kareem (2001, 2003) proposed a time-variant formulation of the impulsive response function modulated by the LF angle of attack. In the wake of this work, Barni et al. (2021, 2022) proposed a 2D rational function approximation to improve the modeling of the experimental aerodynamic derivatives, which is a key point for the accuracy of the procedure.

For all the aforementioned non-linear models, a crucial issue is still represented by the definition of the cutoff frequency, employed to identify the LF range and the HF range of the turbulence spectrum, which, as stated by Wu et al. (2013), could significantly affect the results. As already mentioned, in the framework of the CQST-based approaches, the threshold frequency is typically identified considering a value of V^* at which the flutter derivatives and aerodynamic admittance functions converge to the corresponding quasi-static value. Differently, Chen and Kareem (2001) imposes the limiting frequency equal to the first natural frequency of the structure.

From the literature review provided, it is evident that there is considerable interest among researchers in the nonlinear modeling of wind forces on bridges since, the existing linear approaches, though useful for certain conditions, may not fully capture the intricate effects of turbulence and non-synoptic features.

Extreme climate events, such as thunderstorms and downbursts, are of particular interest due to their strong low-frequency fluctuations of mean wind speed and angle of attack. These events can lead to non-stationary and nonlinear aerodynamic forces acting on the bridge deck. Understanding and accurately modeling the nonlinearities in such conditions is essential for ensuring the safety and resilience of long-span bridges.

In this work, the model proposed by Diana et al. (2013) is revised and updated to account for the low-frequency variation of the wind

speed generated by non-synoptic winds. The storm "Tor", which was monitored on the Hardanger Bridge in Norway in January 2016 (Fenerci and Øiseth, 2018), was considered a good opportunity to preliminary validate the numerical model against full-scale measurements of an extreme weather event. In particular, the time series obtained from the 8 anemometers positioned along the deck are used to generate a wind scenario, which served as input for the updated model. Subsequently, the numerical outcomes are compared to the monitored dynamic response of the bridge deck.

Afterward, the method is applied to two test cases: a super-long span suspension bridge (the Messina Strait Bridge) and a relatively short-span bridge (the Gjemnessund Bridge). Each test case involves the generation of two different wind scenarios to investigate the response of the bridges while considering the nonlinearities of the aerodynamic forces. The first scenario represents a standard synoptic wind synthetically generated. On the other hand, the second wind field is tailored based on the full-scale measurements of the storm "Tor" and it represents an extreme weather event. The research aim is to investigate the response of two different bridges under different wind conditions when accounting for nonlinear aerodynamic forces. The synoptic scenario provides a baseline analysis considering typical wind conditions while, the non-synoptic case, introduces the complexities of turbulent wind with low-frequency variations in wind speed and angle of attack. The nomenclature used in the paper is reported in Table 1.

The paper is structured as follows:

- Section 2 introduces the updated numerical method and its validation through comparison with full-scale measurements on the Hardanger Bridge in Norway during the storm "Tor";
- Section 3 provides details on the bridges selected as test cases and outlines the numerical wind scenarios employed;
- Section 4 presents and discusses the results in detail;
- Finally, in Section 5, conclusions are drawn.

2. Mathematical modeling

2.1. Simulation framework

As previously introduced, the method presented in this paper represents an update of the numerical procedure originally proposed by Diana et al. (2013), which relies on a dual-band superposition approach. The algorithm involves several steps, starting with the definition of a cutoff frequency. Specifically, the low-frequency (LF) response of the bridge is obtained by applying the CQST after low-pass filtering the wind spectrum under the limiting value. By adopting this approach, the CQST can be effectively applied in a range of V^* where it correctly reproduces the aerodynamic forces. Hence, a potential criterion to define the threshold frequency is to identify a corresponding V^* beyond which the flutter derivatives converge towards the related quasi-static values.

Nevertheless, when dealing with climate events such as thunderstorms or downbursts, characterized by a slowly varying longitudinal wind component u, the definition of a cutoff frequency is not straightforward. In contrast to Diana et al. (2013), the updated approach employs a time-variant filter to define the LF wind. Therefore, after selecting a limiting V^*, it is possible to update the cutoff frequency while u gradually changes over time.

Subsequently, the high-frequency (HF) response is computed by linearizing, at each time step, the aerodynamic forces around the LF solution. The method employs rheological models to translate in the time domain the flutter derivatives (FDs) and the aerodynamic admittance functions (AAf) typically expressed as a function of V^* for different static angles of attack. These models consist of simple mechanical oscillators, calibrated to represent the transfer functions associated with self-induced forces and those associated with turbulence-induced forces. As a result, each rheological model receives either a deck displacement or an HF wind component as input and returns to the structure respectively a motion-dependent or a buffeting force.

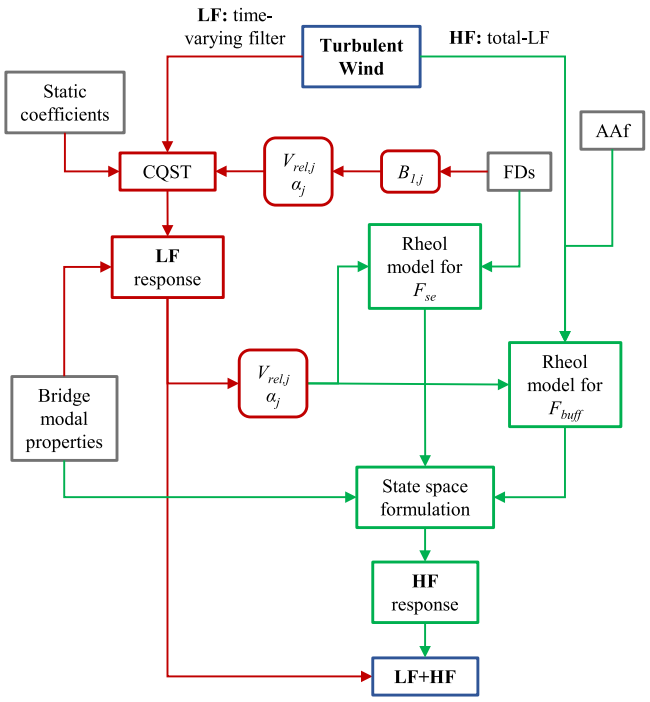

Fig. 1. Flowchart of the updated numerical procedure.

At each time step, the rheological parameters, identified based on experimental flutter derivatives and aerodynamic admittance functions defined around specific static rotations, are linearly interpolated taking into account the LF wind angle. Moreover in the proposed approach, with respect to Diana et al. (2013), the HF forces are modulated also by the LF instantaneous relative velocity.

It is worth mentioning that, as detailed in Diana and Omarini (2020), the inclusion of the rheological models introduces additional degrees of freedom, intended to represent the fluid dynamics of the problem, for each section of the bridge, thereby increasing the computational cost of the simulation. The revised algorithm is illustrated in Fig. 1.

The following sections provide a more detailed description of the method, highlighting the updates that have been introduced.

2.2. LF response: the corrected quasi-steady theory

The computation of the LF response is performed applying the CQST as reported by Diana et al. (1995). In particular, to apply the CQST within a range of V^* where it correctly predicts the aerodynamic forces, the atmospheric wind spectrum undergoes a low-pass filtering process with a predefined cutoff frequency f_{cut}. The threshold value that distinguishes the LF and HF frequency ranges is determined based on the aerodynamic characteristics of the bridge deck section. The criterion involves the selection of a V^*_{cut} value above which the FDs, expressed according to Zasso (1996), almost converge to the quasi-steady limit. Hence, f_{cut} is defined as

$$f_{cut} = \frac{U}{BV^*_{cut}} \tag{1}$$

For instance, examining the flutter derivatives of the Messina Strait Bridge, shown in Fig. 2, an appropriate value of V^*_{cut} could be set equal to 20.

Considering standard synoptic events, the wind flow is generally modeled by superimposing to a steady mean component U an unsteady

fluctuating part. Specifically, U is averaged over a time window of 10 min or 1 h assuming that, in this interval, the wind flow is sufficiently stationary. Consequently, in these scenarios, the definition of f_{cut} is straightforward. However, when dealing with extreme phenomena such as thunderstorms or downbursts, it is not necessarily true that the wind flow is stationary over a 10-minute or 1-hour interval. For instance, Fig. 3(a) shows that the along-wind component $u(t)$, acquired on the Hardanger Bridge in 2016 during the Storm "Tor"(see Fenerci and Øiseth, 2018), strongly changes over 10 min, i.e. between 600 s and 1200 s. In this case, defining a mean wind component U, and thus a "steady" value of f_{cut}, would be incorrect. In this paper, to address this issue, the LF wind is determined using a time-varying linear filter to continuously update f_{cut} over time while keeping a fixed value of V^*_{cut}. This approach allows for a more correct representation of the LF wind which considers the changing nature of extreme atmospheric phenomena.

The first step of the filtering process involves an iterative procedure to define the time-variant $f_{cut}(t)$. Initially, using Eq. (1), a constant value $f_{cut,1}$ is determined by considering a selected V^*_{cut} and, as wind speed, the minimum of the longitudinal component $u_{min,1} = \min u(t)$ of the wind flow to be filtered. The subscript 1 indicates the first iteration step while, the generic integration step, will be denoted by the subscript i. Employing $f_{cut,1} = \frac{u_{min,1}}{BV^*_{cut}}$, it is possible to low-pass filter $u(t)$, defining $u_{LF,1}(t)$. Subsequently, using the minimum value of $u_{LF,1}(t)$, a new cutoff frequency $f_{cut,2}$ can be defined. Therefore, it is possible to low-pass filter again $u_{LF,1}(t)$, starting an iterative procedure. The iteration continues until the difference between $f_{cut,i}$ and $f_{cut,i-1}$ is less than a predefined residual threshold. At this point, using the $u_{LF,i}(t)$ of the last iteration, it is possible to define a time-variant $f_{cut}(t)$, using Eq. (1) as:

$$f_{cut}(t) = \frac{u_{LF,i}(t)}{BV^*_{cut}} \tag{2}$$

Fig. 3(c) shows an example of the $f_{cut}(t)$ resulting following the described procedure, applied to the time–history $u(t)$ in Fig. 3(a), using $V^*_{cut} = 20$.

The second stage of the process involves the filtering of the wind field using the time-variant $f_{cut}(t)$ previously defined. This is done by low-pass filtering the wind time histories $u(t)$ and $w(t)$, through a linear system with time-varying coefficients determined by $f_{cut}(t)$ (e.g. Fig. 3(d)).

Finally, the HF wind is determined by subtracting the LF part from the original time histories (Fig. 3(e)).

According to the CQST, the aerodynamic forces per unit length can be computed as:

$$D(t) = \frac{1}{2}\rho B[V_{rel,D}(t)]^2 C_D(\alpha_D(t)) \tag{3}$$

$$L(t) = \frac{1}{2}\rho B[V_{rel,L}(t)]^2 C_L(\alpha_L(t)) \tag{4}$$

$$M(t) = \frac{1}{2}\rho B^2[V_{rel,M}(t)]^2 C_M(\alpha_M(t)) \tag{5}$$

with C_D, C_L, and C_M respectively drag, lift, and pitch moment coefficients expressed according to the sign convention reported in Fig. 4, ρ air density, $V_{rel,j}(t)$ instantaneous relative wind velocity and $\alpha_j(t)$ instantaneous angle of attack. The j index is introduced in the notation since the Corrected QST accounts for the quasi-steady aerodynamic effects, in the formulations of the relative velocity and of the angle of attack, using the $B_{1,j}$ coefficients, with $j = D, L, M$. Specifically, referring to Fig. 4

$$V^2_{rel,j} = (u_{LF} - \dot{y}_{LF})^2 + (w_{LF} - \dot{z}_{LF} - B_{1,j}\dot{\theta}_{LF})^2 \tag{6}$$

$$\alpha_j = \theta_{LF} + \psi_j = \theta_{LF} + \tan^{-1}\left(\frac{w_{LF} - \dot{z}_{LF} - B_{1,j}\dot{\theta}_{LF}}{u_{LF} - \dot{y}_{LF}}\right) \tag{7}$$

with ψ_j angle of rotation of $V_{rel,j}$ with respect to the horizontal. u_{LF} and w_{LF} are the longitudinal and the vertical component of the incoming low-pass filtered wind, θ_{LF} is the bridge deck rotation, $\dot{\theta}_{LF}$, $\dot{z}_{LF}$ and $\dot{y}_{LF}$ are respectively the velocity of torsional rotation and that related to the vertical and horizontal displacements. The values of $B_{1,j}$ are identified from the flutter derivatives at $V^* > V^*_{cut}$. In particular:

$$\frac{B_{1,D}}{B} = \frac{p^*_2}{p^*_1} \qquad \frac{B_{1,L}}{B} = \frac{h^*_2}{h^*_1} \qquad \frac{B_{1,M}}{B} = \frac{a^*_2}{a^*_1} \tag{8}$$

where p^*_1, p^*_2, h^*_1, h^*_2, a^*_1 and a^*_2 are the flutter derivatives expressed according to Zasso (1996).

2.3. The rheological model

Assuming small oscillations of the instantaneous angle of attack in the HF range, it is possible to linearize the aerodynamic forces around the LF solution. Consequently, these forces can be modeled using the FDs and the AAf, which are commonly identified with wind tunnel tests on bridge deck sectional models at different V^* and static angles of attack (see Fig. 2). The aerodynamic transfer functions defined from these tests are then reproduced in the time domain with rheological models. Specifically, since we are in a linearized framework, the aerodynamic forces can be considered as the superposition of the self-excited forces and of the buffeting forces, i.e.:

$$F_{HF}(t) = F_{se}(V_{rel}, \alpha, \mathbf{x}_{HF}, \dot{\mathbf{x}}_{HF}) + F_{buff}(V_{rel}, \alpha, u_{HF}, w_{HF}) \tag{9}$$

where $\mathbf{x}_{HF}$ and $\dot{\mathbf{x}}_{HF}$ respectively represent the high-frequency displacements and velocities of the bridge deck. Hence, the HF unsteady forces depend on the LF relative velocity and angle of attack and on the HF deck motion and wind turbulence.

In particular, specific rheological models, each composed of several mechanical systems arranged in parallel, are employed to represent in time the transfer functions related to the self-induced forces and those related to the buffeting forces, respectively defined as reported by Diana et al. (2013).

Considering the motion-induced forces, the mechanical systems, structured as shown in Fig. 5, are conceived to receive the motion of the bridge deck as input and generate the corresponding HF force component in response. Consequently, the parameters of the rheological models must be accurately identified to ensure that the resulting transfer function closely matches the experimental aerodynamic transfer function under consideration. As an example, considering a constant wind speed, the self-excited aerodynamic lift per unit length, induced by a torsional motion of the deck around a static angle of attack α_{st}, can be defined as

$$L_\theta(t) = \frac{1}{2}\rho U^2 B\left[h^*_3 - i\frac{2\pi}{V^*}h^*_2\right]\theta(t) = \frac{1}{2}\rho U^2 B[T_{L,\theta}(\alpha_{st})]\theta(t) \tag{10}$$

where $T_{L,\theta}$ is the transfer function between the self-excited lift and θ. $T_{L,\theta}$ is defined using the flutter derivatives h^*_3 and h^*_2, obtained according to the procedure outlined in Diana et al. (2015b). Therefore, it is dependent on α_{st} and $f^* = 1/V^*$.

The identification procedure consists of defining the number and the characteristics of the mechanical oscillators with a constrained optimization which minimizes the difference between the rheological transfer function and the experimental one, defined by Eq. (10), imposing the dynamic stability of the subsystems. Fig. 6 shows the comparison between $T_{L,\theta}$, computed with Eq. (10), and the corresponding rheological transfer function for each α_{st}. Similar rheological models are defined for the other self-induced force components (see for instance Fig. 7, which reports the identification of transfer function $T_{M,\theta}$ for different angles of attack in the case of the Messina Strait Bridge).

In presence of non-synoptic winds, Eq. (10) is implemented as:

$$L_{\theta,HF}(t) = \frac{1}{2}\rho V_{rel,L}(t)^2 B[T_{L,\theta}(\alpha_L(t))]\theta_{HF}(t) \tag{11}$$

where the constant mean wind speed U is replaced by the slowly time-varying $V_{rel,L}(t)$, the mean angle of attack α_{st} is replaced by the slowly

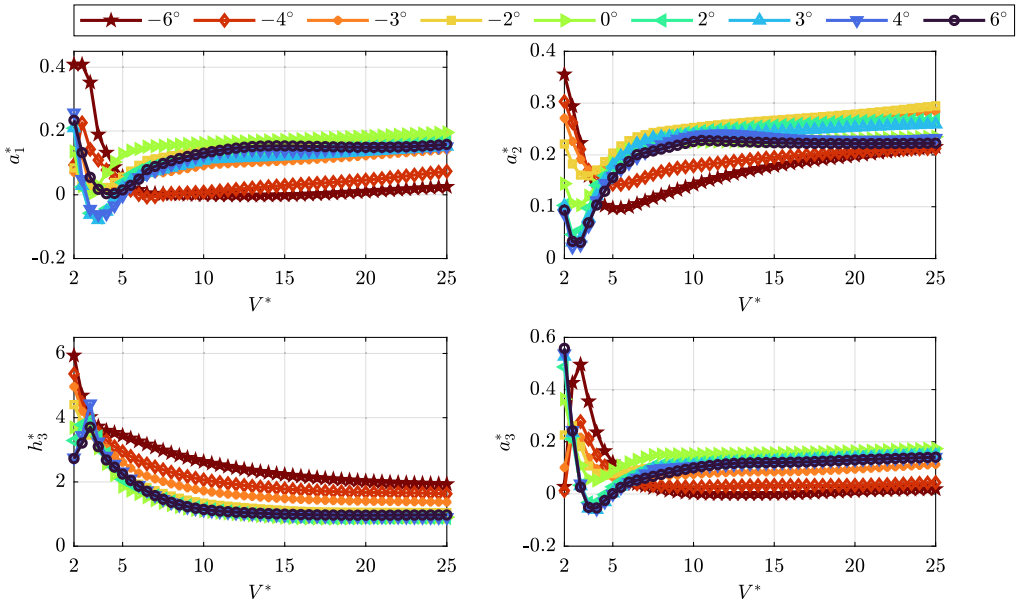

Fig. 2. a_1^*, a_2^*, a_3^* and h_3^* flutter derivatives of the Messina Strait Bridge, identified for different static angles of attack.

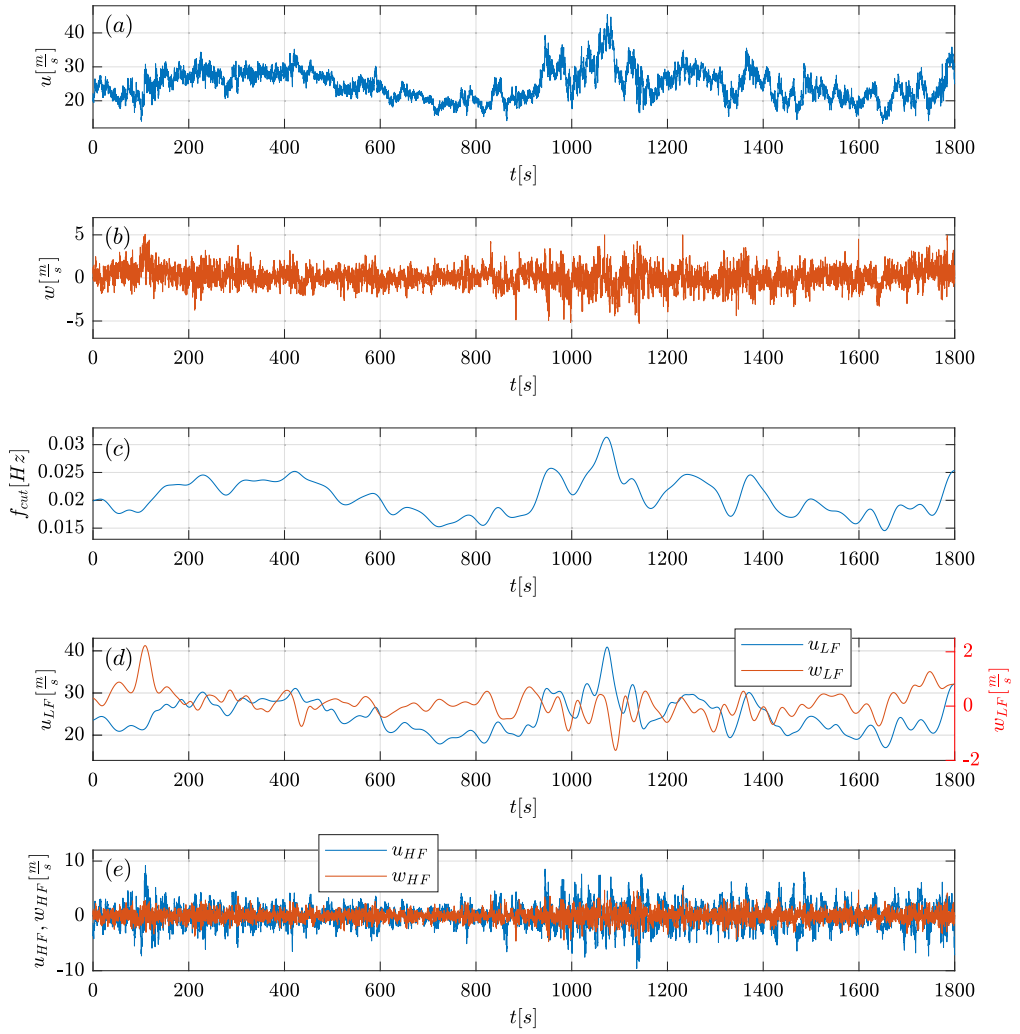

Fig. 3. An example of the application of the time-variant low-pass filter is presented. Figures (a) and (b) display the measured along-wind and vertical components (obtained from the Hardanger Bridge monitoring campaign, see Fenerci and Øiseth, 2018). Figure (c) illustrates the time-variant cutoff frequency defined by using $V_{cut}^* = 20$ and $B = 60\,\text{m}$ (deck chord length of the Messina Strait Bridge). The LF wind is shown in Figure (d). Finally, the HF wind, obtained by subtracting the LF part from the original time histories, is reported in Figure (e).

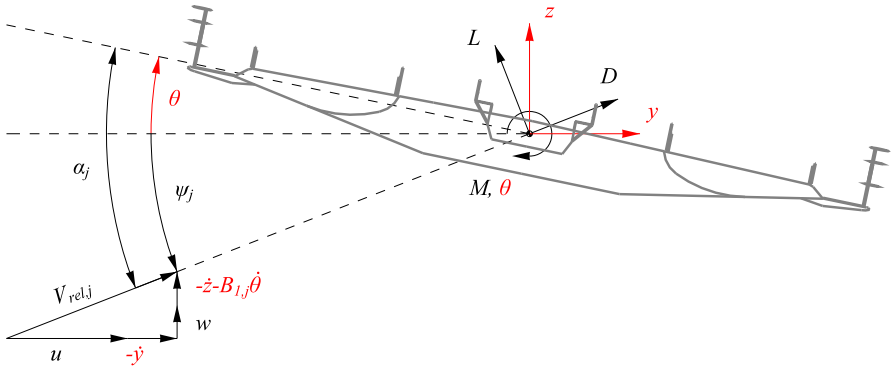

Fig. 4. Sign convention.

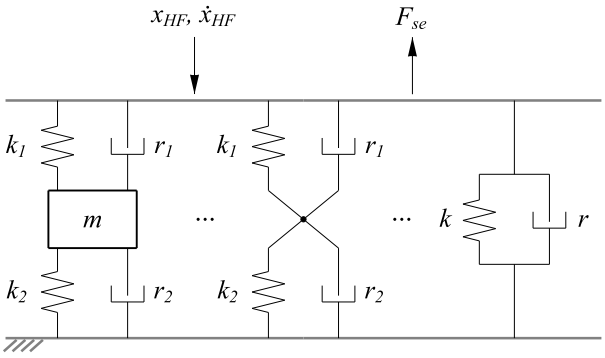

Fig. 5. Sketch of the rheological models employed for the self-excited forces. The mechanical system receives as input the bridge deck HF displacements and velocities and provides as output the selected self-induced force component.

time-varying $\alpha_L(t)$, while θ and L_θ get the subscript HF to highlight their high frequency characteristics.

A similar approach is used for the buffeting forces. In this case, the rheological models take an HF wind velocity component as input and provide the corresponding buffeting force back to the deck. As shown in Fig. 1, once the HF solution is available the total solution is finally computed by superimposing the LF and the HF responses.

As previously mentioned, incorporating rheological models introduces additional degrees of freedom to the original system, thereby expanding the matrices that describe the dynamic problem. The numerical construction of these matrices is thoroughly detailed in Diana and Omarini (2020). This issue becomes even more pronounced when dealing with a full bridge case, as the degrees of freedom added by the identified rheological models must be multiplied by the number of sections into which the deck is subdivided.

2.4. Validation of the numerical method by comparison with full-scale measurements

The validation of numerical models to predict the response of long-span bridges to turbulent winds is a challenging and crucial task. As already mentioned, the rheological model presented is an update of the approach outlined by Diana et al. (2013), which was validated by performing wind tunnel tests wherein the wind angle of attack varied while maintaining a constant velocity. To extend the validation by accounting for the variation of the wind velocity over time, a comparison is performed between numerical results and the full-scale response of a long-span bridge subjected to a non-synoptic wind. The data collected during the storm "Tor", acquired in January 2016 on the Hardanger Bridge in Norway, see Fenerci and Øiseth (2018), is considered suitable to achieve this purpose. The bridge was equipped with 8 anemometers, attached to the hangers at 8 m above the deck girder, and 16 accelerometers positioned in similar longitudinal locations. Fig. 3(a) and 3(b) show the signals recorded from 16:30 to 17:00 by the anemometer "A4", located 200 m away from the bridge mid-span.

Concerning the inputs for numerical simulations, the structural properties of the bridge and the aerodynamic characteristics of the deck are respectively detailed in Barni et al. (2022, 2021). On the other hand, the generation of a non-synoptic wind field, based on full-scale measurements, is not straightforward. In fact, the measured wind angles of attack can be affected by the presence of the deck itself and therefore, specific wind tunnel tests are needed to correct the data (see Diana et al., 2023). Moreover, the proper replication of the time-varying correlation of a non-synoptic wind along the bridge deck is challenging since the measurements are performed at a few specific sections. Finally in this specific case, all the anemometers, except for the "A6", are positioned downstream with respect to the wind direction. Hence, to validate the model despite these uncertainties, a simplified wind scenario is implemented. First, the anemometer measurements are filtered with the procedure reported in Section 2.2 using $V^*_{cut} = 20$. Subsequently, since storms and downbursts can exhibit a strong lateral correlation of the slowly varying wind (see Chen and Letchford, 2006), the low-frequency components are linearly interpolated in the sections interposed to those where the anemometers are located. On the other hand, the high-frequency parts are generated by considering the turbulence characteristics during the gust. To estimate the wind spatial correlation, the measurements of anemometers "A2", "A3", "A4" and "A5" (see Fenerci and Øiseth, 2018), positioned sufficiently close to each other, are used.

Figs. 8(a), 8(b) and 8(c) show the comparison between numerical and full-scale mid-span displacements. The blue and red lines are the displacements obtained by Fast Fourier Transform (FFT) integration respectively of the numerical and experimental accelerations. The gray lines are the numerical displacements including the quasi-static contribution which cannot be detected by accelerometers. As the wind speed increases, i.e. between 900 s and 1100 s (see Fig. 3(a)), the bridge response amplifies in both the experimental and numerical cases. Differences between numerical results and experimental measurements may be due to uncertainties in the estimation of structural parameters, e.g. the modal damping ratio, and in the way in which the wind was generated. Moreover, neglecting the aerodynamic contribution of cables and towers could also affect the final results. Similar consideration can be done for the quarter-span displacements, reported in Figs. 9(a) and 9(b). During the Hardanger Bridge monitoring campaign, at quarter-span only one accelerometer was installed near the edge of the deck. Therefore, to compare experimental and numerical vertical displacements, the latter includes the contribution due to the torsional rotation at the accelerometer position. Concluding, given the amount

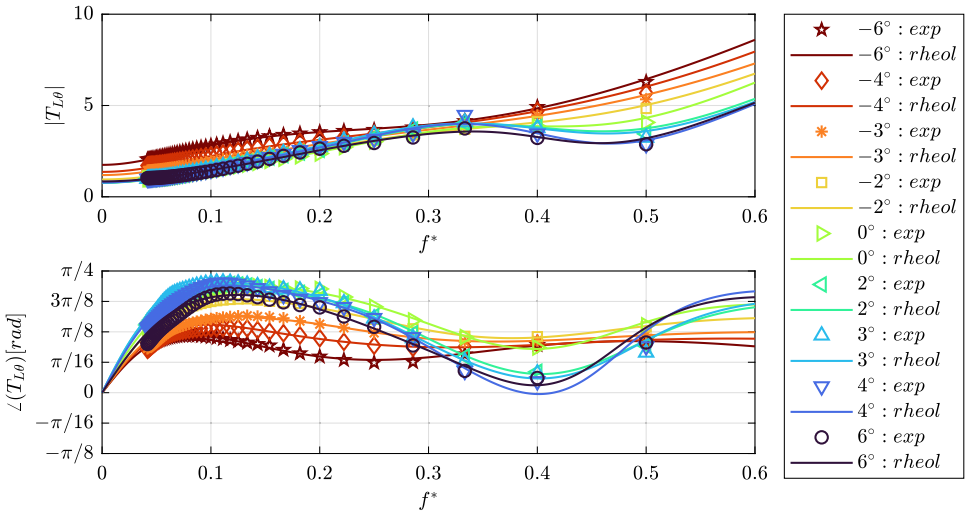

Fig. 6. Comparison of numerical and experimental transfer function $T_{L,\theta}$, as a function of $f^* = 1/V^*$, for different static angles of attack (Messina Strait Bridge).

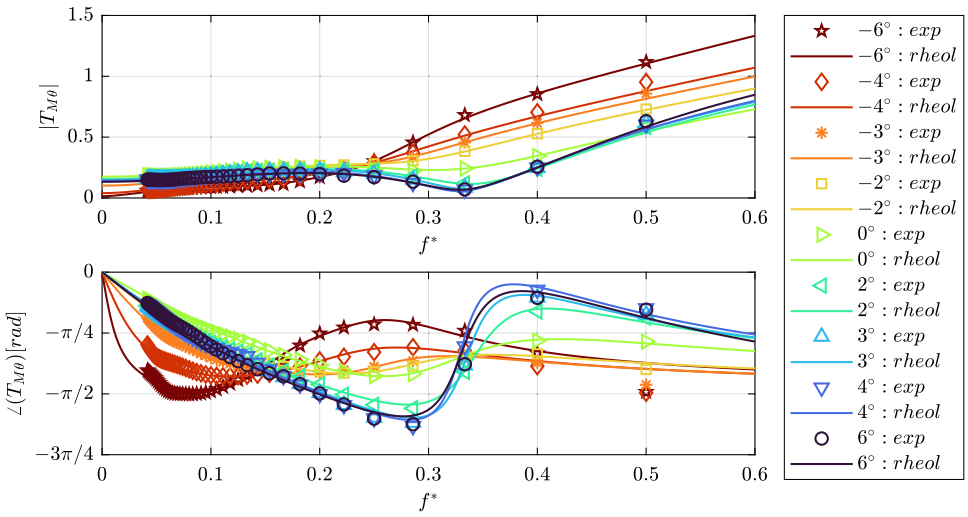

Fig. 7. Comparison of numerical and experimental transfer function $T_{M,\theta}$, as a function of $f^* = 1/V^*$, for different static angles of attack (Messina Strait Bridge).

of uncertainties in the simulation inputs, the comparison between numerical results and full-scale measurements is deemed reasonable. This suggests that the updated method can be applied to investigate the impact of the nonlinearities in the aerodynamic forces on the dynamic response of other bridges.

3. Case studies: The messina strait bridge and the gjemnessund bridge

The method presented is applied to two different case studies: the Messina Strait Bridge and the Gjemnessund Bridge. Two different wind scenarios are applied to both bridges. The first scenario is a standard synoptic wind, generated considering a mean wind speed equal to the design value of the Messina Strait Bridge and the atmospheric turbulence characteristics observed at the construction site.

The second case is generated from a full-scale measurement of the storm "Tor". In particular, the measured wind is scaled to have the same mean wind speed as the synoptic case. This second scenario represents a numerical extreme event characterized by significant low-frequency variations of the wind angle of attack and relative velocity, realized to emphasize the nonlinearities of the aerodynamic forces.

In this section, after briefly reporting the structural properties and the aerodynamic characteristics of the bridges, the generation of the two wind scenarios is discussed in detail.

3.1. Structural properties

The Messina Strait Bridge is a suspended bridge characterized by a main span 3300 m long and a multi-box deck section 60 m wide (see Diana et al., 2013). For the analysis of this research, the first 50 vibration modes and the corresponding modal properties were extracted from a FE model of the structure. These characteristics are deeply detailed in Brancaleoni et al. (2009), Zasso et al. (2013), Argentini et al. (2014).

The second structure examined is the Gjemnessund Bridge, located on the west coast of Norway. This bridge, featuring a main span 623 m long, is relatively short when compared with the Messina Strait Bridge. The deck is characterized by a single-box girder 13.2 m wide. Further specifications can be found in Andersen (2021), Andersen et al. (2022). Again, the structure is numerically modeled considering the first 50 vibration modes (see Diana et al., 2023).

3.2. Aerodynamic properties

The aerodynamic characteristics of both bridges were assessed through dedicated tests carried out in the wind tunnel of Politecnico di Milano (see Diana et al., 2013; Argentini et al., 2014 for more details about the measurements performed on the deck sectional model of the Messina Strait Bridge and Diana et al. (2023) for those related to the

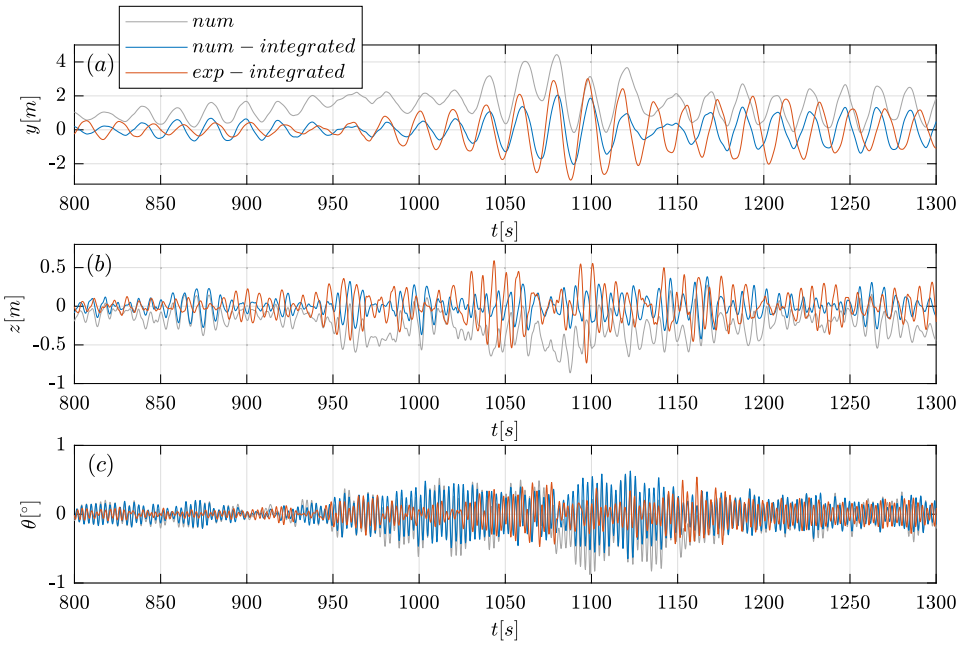

Fig. 8. Comparison between numerical results and full-scale measurements on the Hardanger Bridge ("H5" accelerometers, see Fenerci and Øiseth, 2018). Figures (a), (b) and (c) respectively show the mid-span lateral and vertical displacements and the torsional rotation. The gray lines are the numerical displacements which includes the quasi-static contribution. The blue and red lines are the displacements obtained by FFT integration respectively of the numerical and experimental accelerations.

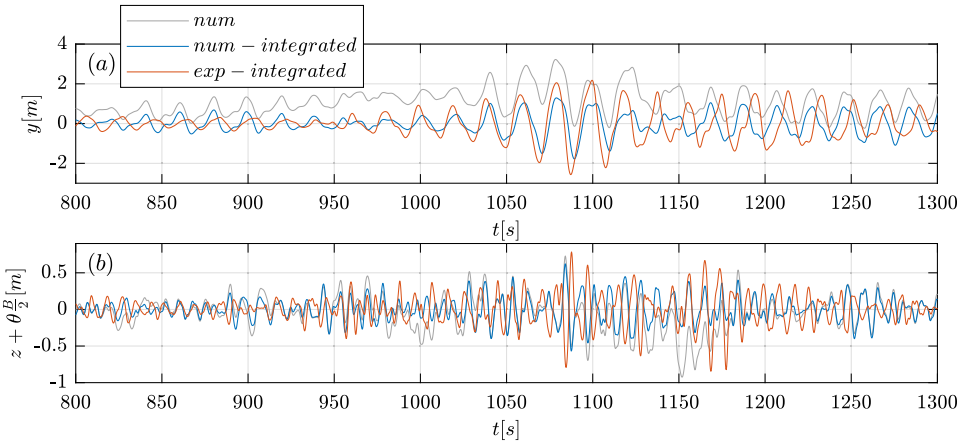

Fig. 9. Comparison between numerical results and full-scale measurements on the Hardanger Bridge ("H8" accelerometer, see Fenerci and Øiseth, 2018). Figures (a) and (b) respectively show the quarter-span lateral displacements and the total vertical displacement at the location of the accelerometer. The gray lines are the numerical displacements which includes the quasi-static contribution. The blue and red lines are the displacements obtained by FFT integration respectively of the numerical and experimental accelerations.

Gjemnessund Bridge). Fig. 10 shows the static aerodynamic coefficients as a function of the wind angle of attack. For the Messina Bridge, a range of angles from −9° to 9° was investigated. In contrast, for the Gjemnessund Bridge, the range was expanded with the specific purpose of being able to simulate atmospheric events characterized by high AoA.

In both cases, the flutter derivatives were determined with forced-motion tests, following the methodology outlined by Diana et al. (2015b). Fig. 2 shows the a_1^*, a_2^*, a_3^* and h_3^* flutter derivatives of the Messina Bridge in a range of reduced velocities between 2 and 25, identified around static angles from −6° to 6°. Similarly, Fig. 11 shows the same coefficients measured on the Gjemnessund Bridge deck sectional model. In this case, the range of V^* is wider, spanning from 2 to 46, but the investigated static angles are more limited compared to the first case. It is worth mentioning that, in the present work, the $B_{1,j}$ coefficients, defined as reported by Eq. (8), are computed considering $V^* = 24$ for the Messina Strait Bridge and $V^* = 40$ for the Gjemnessund Bridge.

3.3. Wind scenarios

Two different wind scenarios are applied to each case of study, aiming to investigate the response of the two structures to different wind fields. It is worth emphasizing that the two wind scenarios are generated to investigate the effect of the nonlinearities in aerodynamic forces, due to low-frequency variations in wind speed and angle of attack, on the dynamic response of the bridges. The characteristics and the generation of these wind scenarios are detailed below.

3.3.1. Scenario A: synoptic wind

The first wind scenario involves a mean wind speed $U = 60\,\mathrm{ms}^{-1}$, which corresponds to the design value of the Messina Strait Bridge (see Brancaleoni et al., 2009). Furthermore, this analysis takes into account the longitudinal and vertical wind turbulence components. The turbulence properties, used to generate the wind fields, are those measured at the construction site of the Messina Bridge. Specifically, Table 2 provides an overview of the parameters employed, including

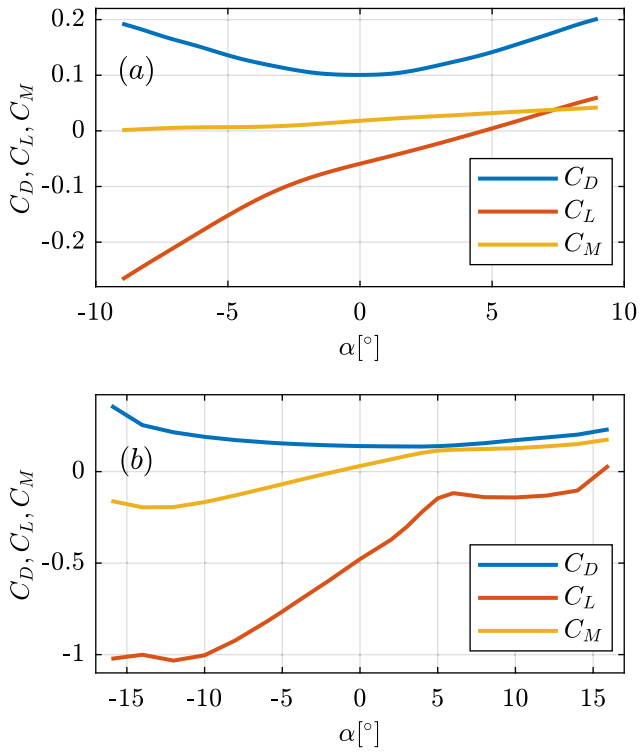

Fig. 10. Static aerodynamic coefficients of the Messina Strait Bridge deck (a) and of the Gjemnessund Bridge deck (b).

Table 2
Parameters employed for the generation of the synoptic wind field.

Mean wind speed	$U = 60$ m s^{-1}
Air density	$\rho = 1.22$ kg m^{-3}
Turbulence intensity	$I_u = 0.10, I_w = 0.05$
Integral length scales	$L_u^x = 200$ m, $L_w^x = 20$ m
u and w spectra	$\frac{f \cdot S_u(f)}{\sigma_u^2} = \frac{4\left(\frac{fL_u^x}{U}\right)}{\left[1+70.8\left(\frac{fL_u^x}{U}\right)^2\right]^{5/6}}$, $\frac{f \cdot S_w(f)}{\sigma_w^2} = \frac{4\left(\frac{fL_w^x}{U}\right)\left[1+755.2\left(\frac{fL_w^x}{U}\right)^2\right]}{\left[1+283.2\left(\frac{fL_w^x}{U}\right)^2\right]}$
uw spectrum	$S_{uw}(f) = 0$

the power spectral densities of the longitudinal and vertical wind components as a function of the frequency f. Moreover, selected two points P and Q, the spatial coherence of u or w is defined as follows

$$\Lambda_{ii} = exp\left(-\frac{2\sqrt{(C_{ix}\Delta x)^2 + (C_{iz}\Delta z)^2}\, f}{U_P + U_Q}\right) \tag{12}$$

with $i = u, w$, $C_{ux}, C_{uz} = 10$, $C_{wx} = 6.5$ and $C_{wz} = 3$. Δx and Δz are respectively the longitudinal and the vertical distances between P and Q.

Finally, the time histories are generated employing a harmonic superposition method (see Shinozuka and Jan, 1972; Deodatis, 1996; Ding et al., 2006). For both structures, the wind time histories are applied to sections defined at a longitudinal distance equal to the deck chord B. This results in 54 time histories generated for the Messina Bridge and 48 time histories for the Gjemnessund Bridge.

3.3.2. Scenario B: non-synoptic wind

The second scenario is derived from measurements recorded during the storm "Tor", which struck the Hardanger Bridge on January 29 and 30, 2016. Specifically, the signals recorded from 16:30 to 17:00 by the anemometer "A4" are used as a starting point for tailoring the wind field (see Figs. 3(a) and 3(b)).

As a first step, the wind components are scaled to reach the same mean wind speed of the synoptic case (see Table 2). The scaling is performed by multiplying $u(t)$ and $w(t)$ by the ratio between the design wind speed of the Messina Bridge, i.e. 60 ms^{-1}, and the average of the original $u(t)$ time history, i.e. 24.7 ms^{-1}. By following this approach, the wind AoA are preserved while, the wind speed, reaches values that could lead, in both cases, to aerodynamic instabilities (see Argentini et al., 2014 and Diana et al., 2023, which respectively report the flutter critical wind speed for the Messina Bridge and the Gjemnessund Bridge).

Subsequently, the LF portion of the wind is defined by filtering the scaled signals following the procedure introduced in Section 2.2. In the case of the Messina Bridge, a limiting V_{cut}^* of 20 is selected, while for the Gjemnessund Bridge, it is set to 25. It is worth mentioning that the flutter derivatives of the Gjemnessund Bridge, measured around a static angle of attack equal to 6°, still change at $V^* > 25$ (see Fig. 11). This divergence persists since, at this AoA, the derivatives of the static lift and moment coefficients approach zero (see Fig. 10(b)). Consequently, the convergence of the flutter derivatives to their corresponding quasi-steady values is not ensured. Fig. 12 reports the scaled LF time series and the related wind angle of attack. On the other hand, the HF range is obtained starting from the wind time histories generated for scenario A, employing the parameters reported in Table 2. Specifically, the HF part of these latter, obtained by applying the filtering procedure reported in Section 2.2, is superimposed to the LF portion previously defined. The resulting time series, applied to the mid-span section of the Messina Strait Bridge, are shown in Fig. 13.

Following this procedure, the LF range remains constant across each section of the bridge while, the HF one, changes along the deck according to the turbulence properties reported in Table 2. Nevertheless, when dealing with storms and downbursts, the slowly varying wind, which represents the large atmospheric scales, can exhibit a strong correlation up to distances exceeding 1000 m (see Chen and Letchford, 2006). Consequently, for the Messina Bridge, the wind is simulated with a constant LF portion over a 1000 m longitudinal window, positioned at the center of the main span. Laterally, the time histories are exponentially reduced until a scaling factor of 0.3 is applied at the towers. For the Gjemnessund Bridge, which is 623 m long, there is no need to scale the wind field.

As a final remark, it is important to note the generated non-synoptic scenario is a simplification of the real atmospheric phenomenon. As detailed in Fenerci and Øiseth (2018) and Tang et al. (2020), the turbulence characteristics vary as a function of the mean wind speed. In contrast, our approach involves the superimposition of the HF part of scenario A to the LF time series. However, the main interest is in the low-frequency variation of the wind speed and angle of attack, since the HF response is calculated by linearizing, at each time step, the aerodynamic forces around the LF solution (see Section 2.3). Therefore, to focus the analysis on this aspect, we generated two wind scenarios wherein the only variable changed was the LF part.

4. Results discussion

The two wind scenarios are applied to both bridges under study, i.e. the Messina Strait Bridge and the Gjemnessund Bridge. The main purpose of the study is to explore the dynamic responses of the two structures subjected to a synoptic and a non-synoptic wind field, previously described in Section 3.3. In this chapter, the results obtained are presented and analyzed.

4.1. Messina strait bridge

Fig. 14 shows the mid-span lateral displacement (a), vertical displacement (b), and torsional rotation (c) of the Messina Strait Bridge. Additionally, the LF relative velocity and angle of attack, both computed using the B_{1M} coefficients as reported by Eq. (8), are depicted respectively in Fig. 14(d) and 14(e). For each plot, a comparison is

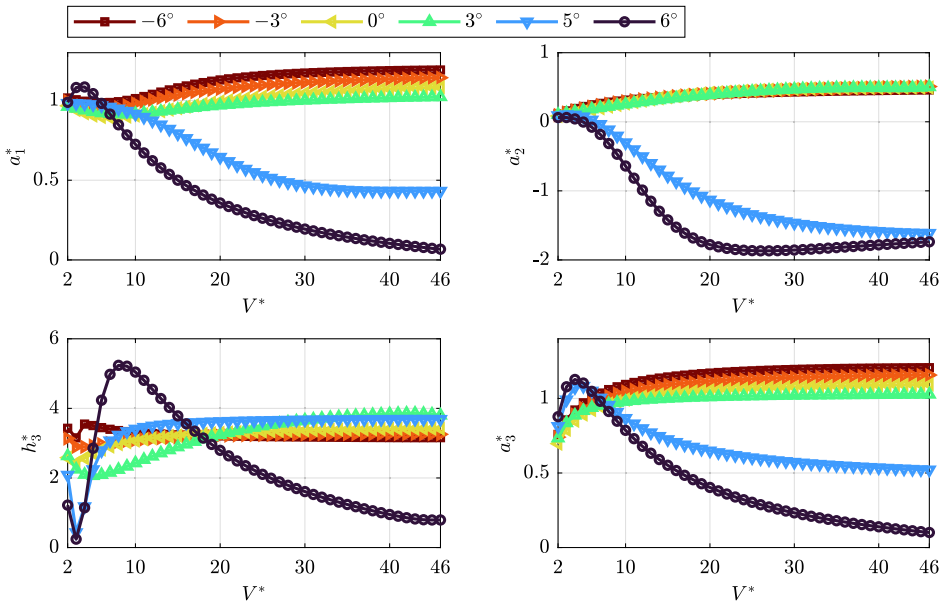

Fig. 11. a_1^*, a_2^*, a_3^* and h_3^* flutter derivatives of the Gjemnessund Bridge, identified for different static angles of attack. According to the definition used (Zasso, 1996), a negative a_2^* represents negative torsional aerodynamic damping.

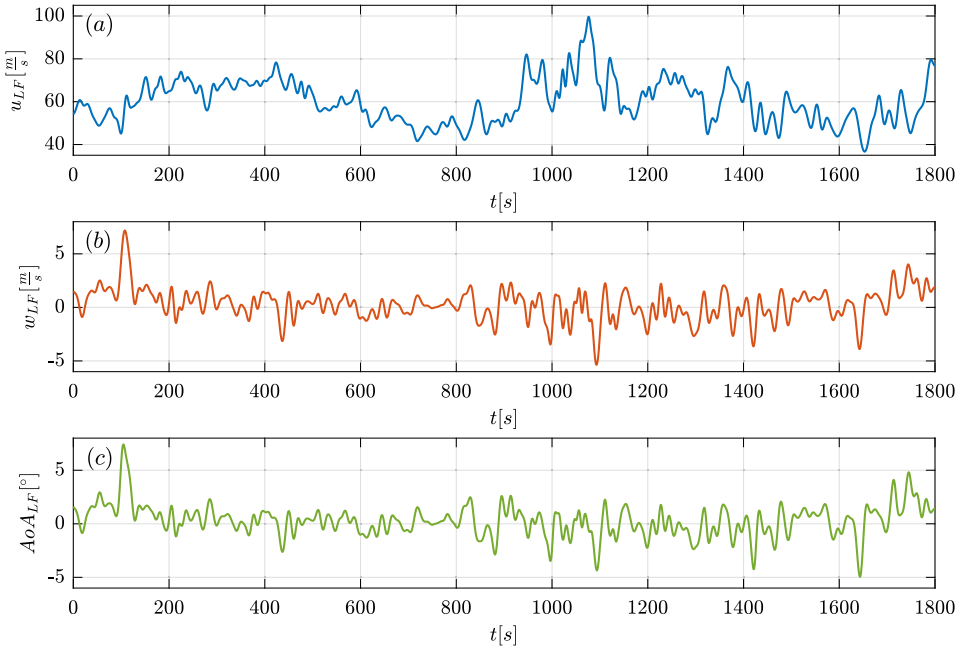

Fig. 12. Along-wind (a) and vertical (b) components scaled and filtered as described in Section 2.2 for the case of the Messina Strait Bridge. Figure (c) reports the related LF wind angle of attack.

made between the response related to the synoptic (scenario A) and the non-synoptic wind field (scenario B).

By comparing the bridge's response in the two cases, it can be noted that referring to scenario B, the slowly varying displacements closely track the trend of $V_{rel,M}$. On the other hand, the synoptic case is characterized by oscillations around a mean value that remains approximately constant over time.

The time window between 900 s and 1200 s (shown in green in Fig. 14) is of particular interest as the non-synoptic LF relative velocity reaches its maximum values. During this period, the bridge response related to scenario B closely mirrors the variations of $V_{rel,M}$, leading to a lateral peak value of 21 m, approximately twice the corresponding displacement observed in case of scenario A. Similar behavior can also be noted looking at the vertical displacement and the torsional rotation. However, these responses are limited to very low values due to the aeroelastic stability of the Messina Bridge. Furthermore, no flutter instability was observed since the wind does not persist above the critical wind speed (i.e. $U_{cr} \simeq 90\,\mathrm{ms}^{-1}$, see Argentini et al., 2014) for a sufficient period.

Another time window of significant interest is between 80 s and 300 s (highlighted in gray in Fig. 14). Within this interval, the non-synoptic LF angle undergoes a transition from nearly 0° to approximately 8° due to the variation of the LF vertical wind component. Simultaneously, a remarkable change in the bridge's response is observed. By comparing to the preceding time instants, the lateral displacement nearly doubles while the vertical one changes in sign. This behavior can be explained

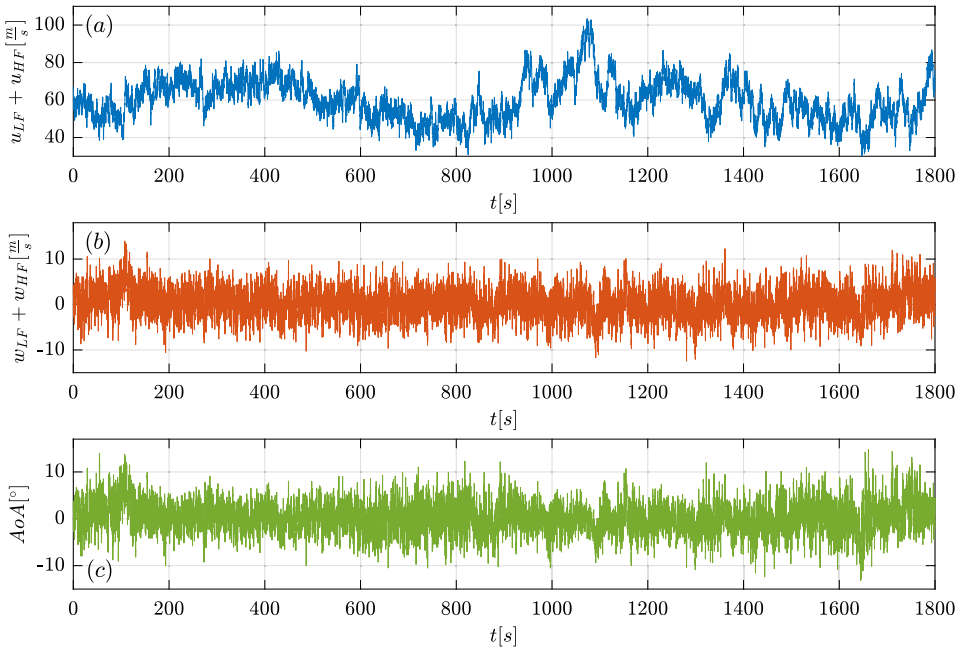

Fig. 13. Final longitudinal (a) and vertical (b) wind components, which characterize scenario B, applied to the mid-span section of the Messina Strait Bridge. Figure (c) reports the related wind angle of attack.

by the variation of α_j, which induces strong changes in the static aerodynamic coefficients (see Fig. 10(a)). Consequently, there is a significant alteration in the LF aerodynamic forces, as shown in Fig. 15.

Finally, it is important to highlight that a significant portion of the dynamic response of this bridge is captured by the CQST since the natural frequencies related to the first modes of vibration of the structure are lower or in close proximity to the frequencies that characterize the LF range of the wind.

4.2. Gjemnessund bridge

The dynamic response of the Gjemnessund Bridge, including mid-span lateral displacement, vertical displacement, and torsional rotation, is illustrated in Fig. 16. As for the Messina Bridge, the response is plotted alongside the LF relative velocity $V_{rel,M}$ and angle of attack α_M for both wind scenario A and scenario B.

Comparing the curves in Figs. 14(e) and 16(e), it can be noted that in the second case, $V_{rel,M}$ and α_M are less filtered than the first one. This discrepancy arises due to the different range of frequencies employed to low-pass filter the incoming wind. Indeed, as reported by Eq. (1), even if V^*_{cut} is similar, the length of the deck chord is significantly different (i.e. $B = 60\,\text{m}$ for the Messina Bridge and $B = 13.2\,\text{m}$ for the Gjemnessund Bridge) and thus, in this case, f_{cut} is higher. On the other hand, the natural frequencies of the Gjemnessund Bridge (see Diana et al., 2023) are much higher than those of the Messina Strait Bridge (see Brancaleoni et al., 2009; Zasso et al., 2013; Argentini et al., 2014) and therefore, a more limited portion of the dynamic response is predicted with the CQST.

Fig. 16 focuses on a time window ranging from 800 s to 1200s. Again, as for the Messina Bridge, looking at the non-synoptic wind scenario, the slowly varying response of the bridge follows the trend of $V_{rel,M}$. In particular, the lateral displacement reaches a peak of 10.5 m while vertically, the bridge lowers to a maximum of 3 m.

Between 1050 s and 1100 s, in the wind scenario B, when the relative velocity reaches its peak, the torsional response of the Gjemnessund Bridge experiences a sudden increase, oscillating from −5° to 10°. This unstable behavior can be attributed to the change in the a^*_2 coefficient (see Fig. 11), which shifts from positive to negative as the static angle increases from 3° to 5°.

A negative value of a^*_2 implies a negative aerodynamic torsional damping. Consequently, when the wind reaches angles approximately equal to 5° in conjunction with high relative velocities, the aeroelastic effects lead to a condition where the total torsional damping becomes negative, resulting in a one-degree of freedom dynamic instability. Moreover, examining Figs. 16(c) and 16(d), within 1050 s and 1100 s where $V_{rel,M}$ is significantly high, whenever α_M overcome 5°, the oscillations of θ significantly increases. In contrast, when $\alpha_M < 5°$, the torsional response is positively damped.

As already mentioned, differently from the Messina Strait Bridge, the Gjemnessund Bridge is characterized by a higher natural frequency associated with the first torsional deck vibration mode, which is considerably above the LF range of the wind. Consequently, this part of the response is primarily influenced by the HF aerodynamic forces. Indeed, the one-degree of freedom dynamic instability observed is due to the presence of negative values of the a^*_2 coefficient, which are reflected in the time domain by the rheological model.

These results, and the underlined aerodynamic mechanism, could be used to explain the behavior recorded by Fenerci et al. (2023) during a recent monitoring campaign of the Gjemnessund Bridge. Although the velocities are much lower and the angle-of-attack was not reported, they present an extreme event where the torsional response was also high and not predictable with standard approaches. More investigations are therefore envisaged to see the applicability of the proposed model, given that the knowledge of the complete wind field along the bridge is still a source of uncertainty.

5. Conclusions

This paper presented a nonlinear approach to simulate the response of long-span bridges subjected to turbulent winds. The research aims to investigate the capability of the method to reproduce the nonlinearities of the aerodynamic forces, mainly due to large variations of the wind speed and angle of attack, which are typical features of extreme atmospheric events such as thunderstorms and downbursts.

The numerical approach was applied to investigate the behavior of two different bridges, i.e. the Messina Strait Bridge and the Gjemnessund Bridge, under two distinct wind scenarios: a standard synoptic wind field and a non-synoptic event.

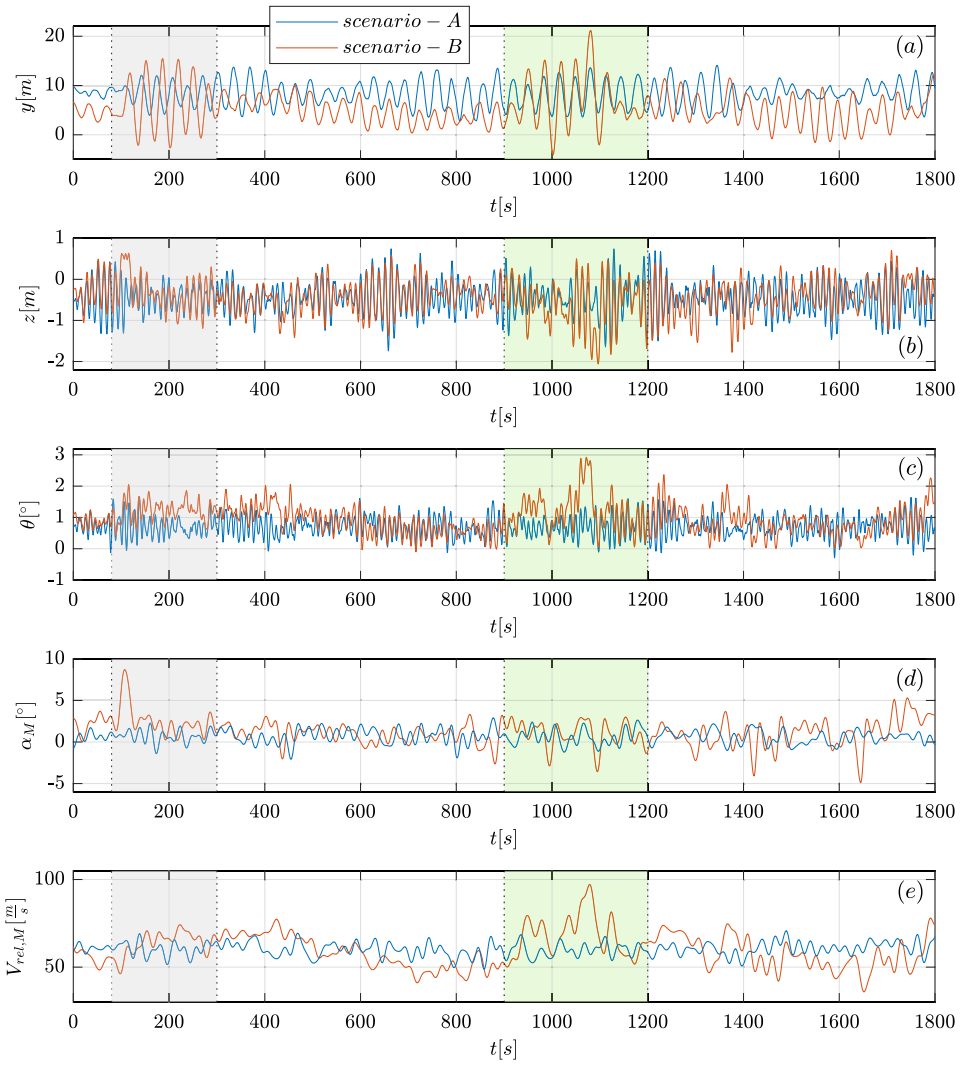

Fig. 14. Mid-span response to wind scenario A (synoptic wind) and B (non-synoptic wind) of the Messina Strait Bridge. Specifically, Figures (a), (b), and (c) respectively show the lateral displacement, the vertical displacement, and the torsional rotation. Figures (d) and (e) report the LF angle of attack α_M and relative velocity $V_{rel,M}$, which modulate the HF response of the bridge.

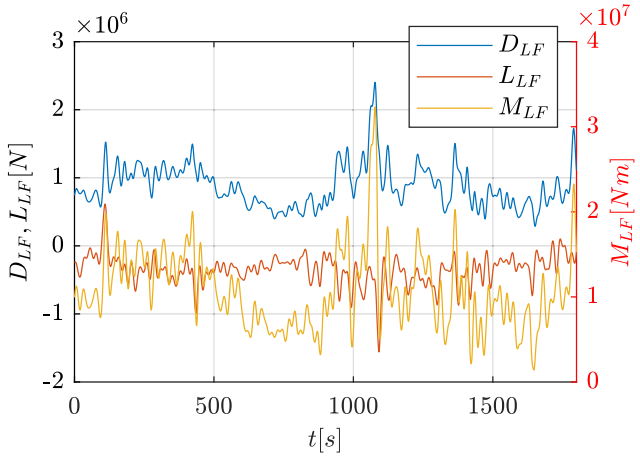

Fig. 15. LF drag, lift, and moment, related to wind scenario B, acting on the mid-span section of the Messina Strait Bridge.

The results obtained from the analysis of the two case studies highlighted that nonlinearities related to the variation of the wind angle of attack could lead to significant changes in the dynamic response of long-span bridges. These effects would have been neglected if standard linearized approaches had been used. The main conclusions drawn from the numerical simulations are summarized below:

- The dynamic response of both bridges appears to effectively track the variations of the wind speed and of the angle of attack, which mainly characterize the non-synoptic wind scenario. On the other hand, as expected, the motion of the bridges under the synoptic wind field remains stable and fluctuates around static values.
- Under the non-synoptic wind scenario, the response of the Messina Strait Bridge is strongly influenced by the LF wind range. In particular, a variation of the angle of attack up to 8° leads to a strong increment of the drag force and thus, to a significant increase in the lateral motion of the bridge. In contrast, the vertical and the torsional motion are limited, without detecting any unstable behavior even if the wind speed reaches values above the flutter limit (i.e., $U_{cr} \simeq 90\,\mathrm{ms}^{-1}$). This is justified by the fact that the wind speed does not persist above the flutter speed one for a sufficient amount of time.
- The dynamic response of the Gjemnessund Bridge, due to the high natural frequencies of the structure, is significantly influenced by the HF aerodynamic forces. Analyzing the non-synoptic scenario,

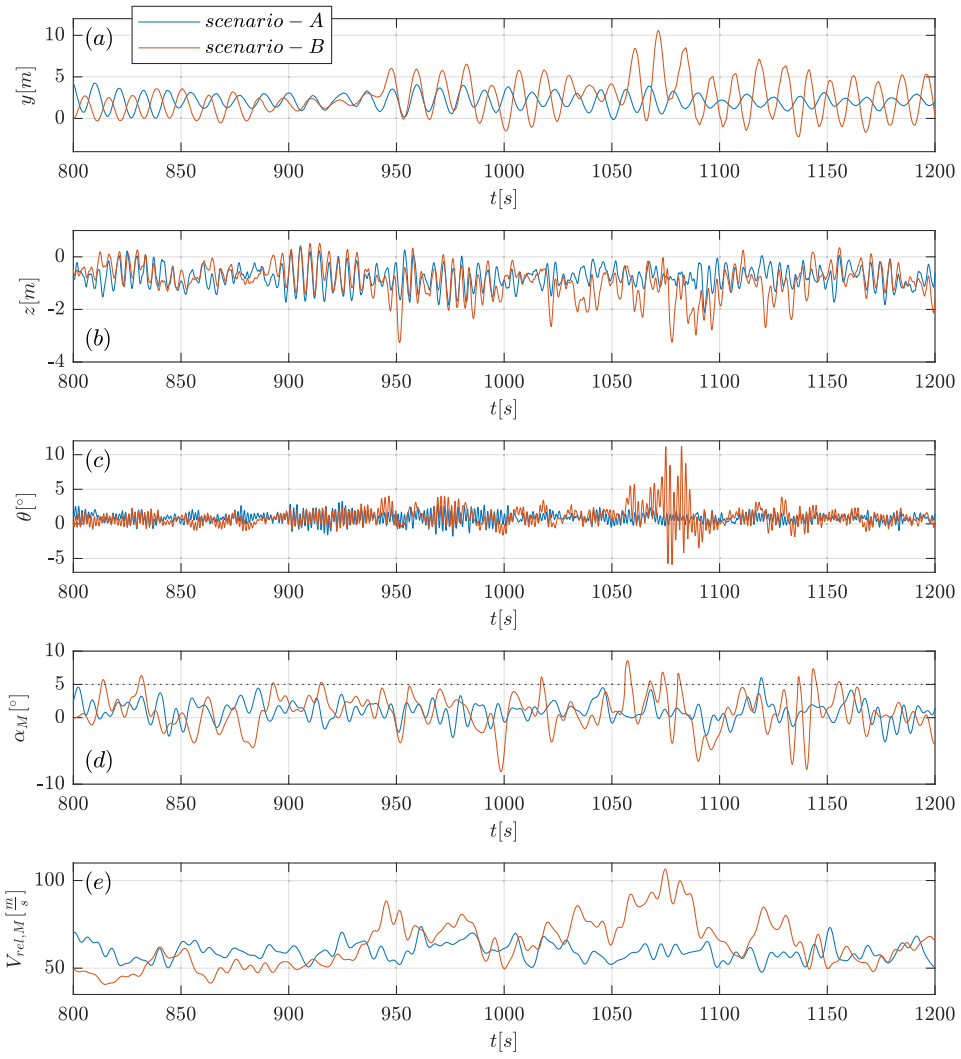

Fig. 16. Mid-span dynamic response of the Gjemnessund Bridge subjected to wind scenario A (synotpic wind) and B (non-synotpic wind). Specifically, Figures (a), (b), and (c) respectively show the lateral displacement, the vertical displacement, and the torsional rotation. Figures (d) and (e) report the LF angle of attack α_M and relative velocity $V_{rel,M}$, which modulate the HF response of the bridge.

a torsional one-degree of freedom instability is excited when the angle of attack approaches 5° at high wind speed. With these angles of attack, the a_2^* coefficient turns negative and leads to this unstable behavior.

CRediT authorship contribution statement

Filippo Calamelli: Conceptualization, Software, Investigation, Formal analysis, Visualization, Writing – original draft. **Roberto Rossi:** Conceptualization, Software, Investigation, Formal analysis, Writing – review & editing. **Tommaso Argentini:** Conceptualization, Methodology, Investigation, Visualization, Writing – review & editing, Supervision. **Daniele Rocchi:** Conceptualization, Methodology, Writing – review & editing, Supervision. **Giorgio Diana:** Conceptualization, Methodology, Writing – review & editing, Supervision.

Declaration of competing interest

The authors declare that they have no known competing financial interests or personal relationships that could have appeared to influence the work reported in this paper.

Data availability

Data will be made available on request.

References

Andersen, M.S., 2021. Operational fluid modal analysis of full-scale pressure and wake flow measurements on the Gjemnessund bridge. Eng. Struct. 249, http://dx.doi.org/10.1016/j.engstruct.2021.113295.

Andersen, M.S., Isaksen, B., Hansen, S.O., 2022. Full-scale monitoring of the wind field, surface pressures and structural response of Gjemnessund suspension bridge. Struct. Eng. Int. 32, 43–54. http://dx.doi.org/10.1080/10168664.2021.1953426.

Argentini, T., Diana, G., Rocchi, D., Somaschini, C., 2016. A case-study of double multimodal bridge flutter: Experimental result and numerical analysis. J. Wind Eng. Ind. Aerodyn. 151, 25–36. http://dx.doi.org/10.1016/j.jweia.2016.01.004.

Argentini, T., Pagani, A., Rocchi, D., Zasso, A., 2014. Monte Carlo analysis of total damping and flutter speed of a long span bridge: Effects of structural and aerodynamic uncertainties. J. Wind Eng. Ind. Aerodyn. 128, 90–104. http://dx.doi.org/10.1016/j.jweia.2014.02.010.

Argentini, T., Rocchi, D., Somaschini, C., 2020. Effect of the low-frequency turbulence on the aeroelastic response of a long-span bridge in wind tunnel. J. Wind Eng. Ind. Aerodyn. 197, http://dx.doi.org/10.1016/j.jweia.2019.104072.

Argentini, T., Rocchi, D., Somaschini, C., Spinelli, U., Zanelli, F., Larsen, A., 2022. Aeroelastic stability of a twin-box deck: Comparison of different procedures to assess the effect of geometric details. J. Wind Eng. Ind. Aerodyn. 220, http://dx.doi.org/10.1016/j.jweia.2021.104878.

Barni, N., Øiseth, O., Mannini, C., 2021. Time-variant self-excited force model based on 2D rational function approximation. J. Wind Eng. Ind. Aerodyn. 211, http://dx.doi.org/10.1016/j.jweia.2021.104523.

Barni, N., Øiseth, O.A., Mannini, C., 2022. Buffeting response of a suspension bridge based on the 2D rational function approximation model for self-excited forces. Eng. Struct. 261, http://dx.doi.org/10.1016/j.engstruct.2022.114267.

Brancaleoni, F., Diana, G., Faccioli, E., Fiammenghi, G., Firth, I.P., Gimsing, N.J., Jamiolkowski, M., Sluszka, P., Solari, G., Valensise, G., Vullo, E., 2009. The Messina Strait Bridge. CRC Press, http://dx.doi.org/10.1201/9781482266368.

Burlando, M., Romanic, D., Solari, G., Hangan, H., Zhang, S., 2017. Field data analysis and weather scenario of a downburst event in Livorno, Italy, on 1 october 2012. Mon. Weather Rev. 145, 3507–3527. http://dx.doi.org/10.1175/MWR-D-17-0018.1.

Caracoglia, L., Jones, N.P., 2003. Time domain vs. frequency domain characterization of aeroelastic forces for bridge deck sections. J. Wind Eng. Ind. Aerodyn. 91, 371–402. http://dx.doi.org/10.1016/s0167-6105(02)00399-9.

Chen, X., Kareem, A., 2001. Nonlinear response analysis of long-span bridges under turbulent winds. J. Wind Eng. Ind. Aerodyn. 89, 1335–1350. http://dx.doi.org/10.1016/s0167-6105(01)00147-7.

Chen, X., Kareem, A., 2003. Aeroelastic analysis of bridges: Effects of turbulence and aerodynamic nonlinearities. J. Eng. Mech. 129, 885–895. http://dx.doi.org/10.1061/ASCE0733-93992003129:8885.

Chen, L., Letchford, C., 2006. Multi-scale correlation analyses of two lateral profiles of full-scale downburst wind speeds. J. Wind Eng. Ind. Aerodyn. 94, 675–696. http://dx.doi.org/10.1016/j.jweia.2006.01.021.

Chen, X., Matsumoto, M., Kareem, A., 2000. Time domain flutter and buffeting response analysis of bridges. J. Eng. Mech. http://dx.doi.org/10.1061/(asce)0733-9399(2000)126:1(7).

Davenport, A., 1962. Buffeting of a suspension bridge by storm winds. J. Struct. Div. ASCE 3, 233–268. http://dx.doi.org/10.1061/jsdeag.0000773.

Deodatis, G., 1996. Simulation of ergodic multivariate stochastic processes. J. Eng. Mech. 122, 778–787. http://dx.doi.org/10.1061/(ASCE)0733-9399(1996)122:8(778).

Diana, G., Amerio, L., Andersen, M.S., Argentini, T., Calamelli, F., Montoya, M.C., de Ville, V., Hernández, S., Jurado, J.Á., Kavrakov, I., Larose, G., Larsen, A., Morgenthal, G., Rocchi, D., Rossi, R., Svendsen, M., Wu, T., 2023. New challenges in the IABSE TG3.1 benchmark on super long span bridge aerodynamics. In: Istanbul IABSE Symposium. Istanbul, pp. 285–293. http://dx.doi.org/10.2749/istanbul.2023.0285.

Diana, G., Falco, M., Bruni, S., Cigada, A., Larose, G.L., Damsgaard, A., Collina, A., 1995. Comparisons between wind tunnel tests on a full aeroelastic model of the proposed bridge over Stretto di Messina and numerical results. J. Wind Eng. Ind. Aerodyn. 54, 101–113. http://dx.doi.org/10.1016/0167-6105(94)00034-b.

Diana, G., Omarini, S., 2020. A non-linear method to compute the buffeting response of a bridge validation of the model through wind tunnel tests. J. Wind Eng. Ind. Aerodyn. 201, http://dx.doi.org/10.1016/j.jweia.2020.104163.

Diana, G., Resta, F., Rocchi, D., 2008. A new numerical approach to reproduce bridge aerodynamic non-linearities in time domain. J. Wind Eng. Ind. Aerodyn. 96, 1871–1884. http://dx.doi.org/10.1016/j.jweia.2008.02.052.

Diana, G., Rocchi, D., Argentini, T., 2013. An experimental validation of a band superposition model of the aerodynamic forces acting on multi-box deck sections. J. Wind Eng. Ind. Aerodyn. 113, 40–58. http://dx.doi.org/10.1016/j.jweia.2012.12.005.

Diana, G., Rocchi, D., Argentini, T., 2015a. Buffeting response of long span bridges: Numerical-experimental validation of fluid-structure interaction models. In: IABSE Conference, Geneva 2015: Structural Engineering: Providing Solutions to Global Challenges - Report. International Association for Bridge and Structural Engineering (IABSE), pp. 2141–2147. http://dx.doi.org/10.2749/222137815818359618.

Diana, G., Rocchi, D., Argentini, T., Muggiasca, S., 2010. Aerodynamic instability of a bridge deck section model: Linear and nonlinear approach to force modeling. J. Wind Eng. Ind. Aerodyn. 98, 363–374. http://dx.doi.org/10.1016/j.jweia.2010.01.003.

Diana, G., Rocchi, D., Belloli, M., 2015b. Wind tunnel: A fundamental tool for long-span bridge design. Struct. Infrast. Eng. 11, 533–555. http://dx.doi.org/10.1080/15732479.2014.951860.

Diana, G., Stoyanoff, S., Aas-Jakobsen, K., Allsop, A., Andersen, M., Argentini, T., Montoya, M.C., Hernàndez, S., Jurado, J.Á., Katsuchi, H., Kavrakov, I., Kim, H.K., Larose, G., Larsen, A., Morgenthal, G., Øiseth, O., Omarini, S., Rocchi, D., Svendsen, M., Wu, T., 2020a. IABSE task group 3.1 benchmark results. Part 1: Numerical analysis of a two-degree-of-freedom bridge deck section based on analytical aerodynamics. Struct. Eng. Int. 30, 401–410. http://dx.doi.org/10.1080/10168664.2019.1639480.

Diana, G., Stoyanoff, S., Aas-Jakobsen, K., Allsop, A., Andersen, M., Argentini, T., Montoya, M.C., Hernàndez, S., Jurado, J.Á., Katsuchi, H., Kavrakov, I., Kim, H.K., Larose, G., Larsen, A., Morgenthal, G., Øiseth, O., Omarini, S., Rocchi, D., Svendsen, M., Wu, T., 2020b. IABSE task group 3.1 benchmark results. Part 2: Numerical analysis of a three-degree-of-freedom bridge deck section based on experimental aerodynamics. Struct. Eng. Int. 30, 411–420. http://dx.doi.org/10.1080/10168664.2019.1661331.

Diana, G., Stoyanoff, S., Allsop, A., Amerio, L., Andersen, M.S., Argentini, T., Calamelli, F., Montoya, M.C., de Goyet, V.d., Hernàndez, S., Jurado, J.Á., Kavrakov, I., Larose, G., Larsen, A., Morgenthal, G., Rocchi, D., Svendsen, M.N., Wu, T., 2022. IABSE task group 3.1 benchmark results. Numerical full bridge stability and buffeting simulations. Struct. Eng. Int. http://dx.doi.org/10.1080/10168664.2022.2104188.

Ding, Q., Zhu, L., Xiang, H., 2006. Simulation of stationary Gaussian stochastic wind velocity field. Wind Struct. 9, 231–243. http://dx.doi.org/10.12989/was.2006.9.3.231.

Fenerci, A., Lystad, T.M., Øiseth, O., 2023. Full-scale monitored wind and response characteristics of a suspension bridge compared with wind tunnel investigations at the design stage. J. Wind Eng. Ind. Aerodyn. 242, 105583. http://dx.doi.org/10.1016/j.jweia.2023.105583.

Fenerci, A., Øiseth, O., 2018. Strong wind characteristics and dynamic response of a long-span suspension bridge during a storm. J. Wind Eng. Ind. Aerodyn. 172, 116–138. http://dx.doi.org/10.1016/j.jweia.2017.10.030.

Hao, J., Wu, T., 2017. Nonsynoptic wind-induced transient effects on linear bridge aerodynamics. J. Eng. Mech. 143, (9), http://dx.doi.org/10.1061/(ASCE)EM.1943-7889.0001313.

Jain, A., Jones, N., Scanlan, R., 1996. Coupled flutter and buffeting analysis of long-span bridges. J. Struct. Eng. 122, 716–725. http://dx.doi.org/10.1061/(asce)0733-9445(1996)122:7(716).

Katsuchi, H., Jones, N., Scanlan, R., 1999. Multimode coupled flutter and buffeting analysis of the Akashi-Kaikyo bridge. J. Struct. Eng. 125, (1), 60–69. http://dx.doi.org/10.1061/(asce)0733-9445(1999)125:1(60).

Kavrakov, I., Legatiuk, D., Gürlebeck, K., Morgenthal, G., 2019. A categorical perspective towards aerodynamic models for aeroelastic analyses of bridge decks. R. Soc. Open Sci. 6 (3), http://dx.doi.org/10.1098/rsos.181848.

Kavrakov, I., Morgenthal, G., 2017. A comparative assessment of aerodynamic models for buffeting and flutter of long-span bridges. Engineering 3 (6), 823–838. http://dx.doi.org/10.1016/j.eng.2017.11.008.

Minh, N.N., Miyata, T., Yamada, H., Sanada, Y., 1999. Numerical simulation of wind turbulence and bu!eting analysis of long-span bridges. J. Wind Eng. Ind. Aerodyn. 83, 301–315. http://dx.doi.org/10.1016/s0167-6105(99)00080-x.

Montoya, M., Hernández, S., Nieto, F., Kareem, A., 2020. Aero-structural design of bridges focusing on the buffeting response: Formulation, parametric studies and deck shape tailoring. J. Wind Eng. Ind. Aerodyn. 204, http://dx.doi.org/10.1016/j.jweia.2020.104243.

Øiseth, O., Rönnquist, A., Sigbjörnsson, R., 2010. Simplified prediction of wind-induced response and stability limit of slender long-span suspension bridges based on modified quasi-steady theory: A case study. J. Wind Eng. Ind. Aerodyn. 98, 730–741. http://dx.doi.org/10.1016/j.jweia.2010.06.009.

Øiseth, O., Rönnquist, A., Sigbjörnsson, R., 2012. Finite element formulation of the self-excited forces for time-domain assessment of wind-induced dynamic response and flutter stability limit of cable-supported bridges. Finite Elem. Anal. Des. 50, 173–183. http://dx.doi.org/10.1016/j.finel.2011.09.008.

Øiseth, O., Sigbjörnsson, R., 2011. An alternative analytical approach to prediction of flutter stability limits of cable supported bridges. J. Sound Vib. 330, 2784–2800. http://dx.doi.org/10.1016/j.jsv.2010.12.026.

Scanlan, R., 1987. On flutter and buffeting mechanisms in long-span bridges. In: Lecture Notes in Engineering. Springer, Berlin Heidelberg, pp. 371–387. http://dx.doi.org/10.1016/0266-8920(88)90004-5.

Shinozuka, M., Jan, C.-M., 1972. Digital simulation of random processes and its applications. J. Sound Vib. 25, 111–128. http://dx.doi.org/10.1016/0022-460X(72)90600-1.

Skyvulstad, H., Argentini, T., Zasso, A., Øiseth, O., 2021a. Nonlinear modelling of aerodynamic self-excited forces: An experimental study. J. Wind Eng. Ind. Aerodyn 209, http://dx.doi.org/10.1016/j.jweia.2020.104491.

Skyvulstad, H., Petersen, Ø., Argentini, T., Zasso, A., Øiseth, O., 2021b. The use of a laguerrian expansion basis as Volterra kernels for the efficient modeling of nonlinear self-excited forces on bridge decks. J. Wind Eng. Ind. Aerodyn 219, http://dx.doi.org/10.1016/j.jweia.2021.104805.

Skyvulstad, H., Petersen, Ø.W., Argentini, T., Zasso, A., Øiseth, O., 2023. Regularised volterra series models for modelling of nonlinear self-excited forces on bridge decks. Nonlinear Dyn. http://dx.doi.org/10.1007/s11071-023-08527-2.

Stoyanoff, S., 2001. A unified approach for 3D stability and time domain response analysis with application of quasi-steady theory. J. Wind Eng. Ind. Aerodyn. 89, 1591–1606. http://dx.doi.org/10.1016/s0167-6105(01)00157-x.

Tang, H., Li, Y., Shum, K., Xu, X., Tao, Q., 2020. Non-uniform wind characteristics in mountainous areas and effects on flutter performance of a long-span suspension bridge. J. Wind Eng. Ind. Aerodyn. 201, 104177. http://dx.doi.org/10.1016/j.jweia.2020.104177.

Wang, H., Wu, T., Tao, T., Li, A., Kareem, A., 2016. Measurements and analysis of non-stationary wind characteristics at Sutong bridge in Typhoon Damrey. J. Wind Eng. Ind. Aerodyn. 151, 100–106. http://dx.doi.org/10.1016/j.jweia.2016.02.001.

Wu, T., Kareem, A., 2014. Simulation of nonlinear bridge aerodynamics: A sparse third-order Volterra model. J. Sound Vib. 333 (1), 178–188. http://dx.doi.org/10.1016/j.jsv.2013.09.003.

Wu, T., Kareem, A., Ge, Y., 2013. Linear and nonlinear aeroelastic analysis frameworks for cable-supported bridges. Nonlinear Dynam. 74, 487–516. http://dx.doi.org/10.1007/s11071-013-0984-7.

Zasso, A., 1996. Flutter derivatives: Advantages of a new representation convention. J. Wind Eng. Ind. Aerodyn. 60, 35–47. http://dx.doi.org/10.1016/0167-6105(96)00022-0.

Zasso, A., Stoyanoff, S., Diana, G., Vullo, E., Khazem, D., Serzan, K., Pagani, A., Argentini, T., Rosa, L., Dallaire, P.O., 2013. Validation analyses of integrated procedures for evaluation of stability, buffeting response and wind loads on the Messina bridge. J. Wind Eng. Ind. Aerodyn. 122, 50–59. http://dx.doi.org/10.1016/j.jweia.2013.07.013.

Zhou, R., Ge, Y., Yang, Y., Du, Y., Zhang, L., 2018. Wind-induced nonlinear behaviors of twin-box girder bridges with various aerodynamic shapes. Nonlinear Dynam. 94 (2), 1095–1115. http://dx.doi.org/10.1007/s11071-018-4411-y.